Contributions to Geophysics and Geodesy Vol. 55/4, 2025 (445–484)

Exploring mineralisation potential using geophysical, remote sensing and field studies in parts of the Migmatite-Gneiss complex, Kwara State, Nigeria

Abdullah Musa ALI*, Ahmed Alhassan AMINU

Department of Geology, Faculty of Earth and Environmental Sciences, Bayero University, PMB 3011, Gwarzo Road, Kano, Nigeria;
e-mail: amali.geo@buk.edu.ng

Abstract: Gold mineralisation and enrichment of critical minerals can be found in placers and veins in the schist belts of the western part of Nigeria. The study area, Bielesin, Asa in Kwara State, experiences a preponderance of artisanal mining that targets the primary gold-quartz presence and associated alluvial occurrences due to the lack of any methodical exploration and development. Hence, this study focuses on preliminary exploration in the study area, which entails identifying geological indicators of mineralisation, and deploying gravity survey and remote sensing investigations to determine potential mineralisation structures. Geochemical analysis was utilised to determine the trace elemental composition of the samples. Vertical electrical sounding (VES) was used to ascertain the thickness of the deposit. The identified minerals in the migmatite gneiss include quartz, feldspar and tourmaline. The observed folded gneissose foliation, schollen and stromatic folds, pegmatites and quartzo-feldspathic veins, and lenses of biotite are indicative of anatexis, which allows for the formation of pegmatites. The valuable minerals occur as discrete grains disseminated in pegmatite and veins. The geological controls for the hosting and emplacement of the mineralisation are structural (faults, fractures). Several features were detected in the study area that could serve as structural controls for ore deposition from hydrothermal solutions or ascending magmatic intrusions. From the interpretation of 3D Euler deconvolution and resistivity results as well as the trenching, the potential auriferous mineralised zones extend from the low-lying quartz veins and pegmatites at depths of approximately 1 m to deep-seated mineralisations at >1000 m. This could help in tonnage estimation and the determination of equipment requirements for excavation activities. This study suggests the presence of gold mineralisation in the study area.

Key words: migmatite gneiss, Bouguer anomaly map, faults and fractures, Landsat imaging, lineaments, pegmatites and quartz veins, vertical electrical sounding

*corresponding author, e-mail: amali.geo@buk.edu.ng

doi: 10.31577/congeo.2025.55.4.3

1. Introduction

The rise in the demand for precious metals and industrial materials undoubtedly shows the relationship between mineral extraction and economic growth. The availability of critical metals to meet the demand of strategic products is a prerequisite factor for any economy to assess its resources. This is to ensure that the future generation is not excluded from the current economic transition in the ever-expanding population. Geophysical techniques have been extensively used to explore mineral resources (*Abdelrahman et al., 2023; Eldosouky et al., 2024a*). Using high-resolution potential field (HRPF) data, *Ekwok et al. (2022)* revealed that igneous intrusions and associated hydrothermal fluids are responsible for brine generation in southeast Nigeria. *Eldosouky et al. (2022)* produced a new subsurface structural map to decipher the structural framework controls on the distribution of gold deposits in Saudi Arabia by applying gravity data to delineate lateral boundaries of subsurface density bodies, and edge detection of potential field data.

However, rather than relying on a single geophysical technique, a combination of two or more geophysical data interpretations can expand the understanding of subsurface geology structures (*Eldosouky et al., 2023*). For instance, *Elkhateeb et al. (2021)* identified potential sites of ore mineral deposits in the southeastern desert of Egypt using aeromagnetic data analysis through the Centre for Exploration Targeting (CET) grid and porphyry analysis techniques. Afterwards, *Hamimi et al. (2023)* integrated potential field- and structural data to trace surface and subsurface large-scale geological structures of the Egyptian Nubian Shield (ENS). The Northern Eastern Desert (NED) of the ENS was found to be dominated by relatively younger (c. 580 Ma) E–W and NE–SW trending extensional structures. The study reported that gravity data are more appropriate in delineating the structural trends compared to the magnetic data which are largely affected by lithological variations and/or alteration zones and magnetic mineralogy.

Over time, remote sensing has been combined with geophysical data to improve the identification of potential mineralisation. *Eldosouky et al. (2024b)* integrated Landsat-9 images and geophysical magnetic data to explore the mineralisation potential of the Egyptian Eastern Desert. By using Principal Component (PC) analysis, Minimum Noise Fraction (MNf) trans-

form, and Band-Ratio (B-Ratio), the study mapped lithological units, hydrothermal alteration regions, and structural elements. The B-Ratio exhibited superior lithological unit identification. *Bencharef et al. (2022)* mapped and predicted potential polymetallic mineralisation locations in Northeastern Algeria by integrating remote sensing, gravity, and magnetic datasets. High zones of lead-zinc mineralisation were identified. *Alarifi et al. (2024)* identified and mapped the hydrothermal alteration zones and structural lineaments that control the mineral occurrences in the Nuqrah region of the Kingdom of Saudi Arabia using remote sensing and aeromagnetic data.

The mineral occurrences of metallic ores (gold, cassiterite, columbite, tantalite and rare-earth metals) are spatially distributed all over Kwara State, which hold promise for further probing and commercial development due to their potentially large reserves (*Dada and Ajadi, 2018*). Gold mineralisation can be found in both eluvial and alluvial placers, and pegmatites and primary veins in the schist belts in the western part of Nigeria (*Garba, 2003*). A number of studies have been performed to improve the understanding of the geological and structural complexities of Kwara State. For instance, using aeromagnetic data, *Balogun (2019)* determined that the presence of major fractures interfered with metamorphic processes in the Ilorin area of Kwara, which influenced the metamorphic grades of the Migmatite–Gneiss–Quartzite complex. This study focuses on the Bielesin area of Asa local government area. The geology of the study area comprises crystalline rock formations, as depicted in Fig. 1. These rocks consist of the migmatitic gneiss complex (MGC), quartzite, mica schist, granodiorite, alkali granite, pegmatite/aplite and vein quartz (*Oyawoye, 1972; McCurry, 1976; Odeyemi, 1981; Ajibade et al., 1987; Adekoya, 1991,* and *Adekoya et al., 2003*). The metamorphic imprints in the archetypical rocks are indicative of the different scales of deformation they have been subject to. The area is part of the southern extension of the northwestern end of the Yauri goldfield, resultant from the development of the Pan-African, intercontinental Anka-Yauri-Iseyin (AYI) transcurrent fault (*Ajadi et al., 2018*).

However, a major constraint in the development of the solid mineral sector in Kwara State is the non-existence of policies for natural resource development. Due to the lack of methodical approaches to exploration, the study area is currently experiencing a preponderance of artisanal mining that targets both the primary gold-quartz presence and their related allu-

vial occurrences (*Ajadi et al., 2018*). This has led to obvious dry exploration pits and burrows, and wasted tailings, resulting in environmental degradation with little or no benefits. It is anticipated that resolving the challenge of inadequate geo-science data through detailed exploration will help to accurately delineate the areas of possible mineral deposits. Therefrom, based on increased confidence and reduced levels of uncertainties, intending investors and miners can securely invest using such data. Hence, this study focuses on preliminary exploration of the study area, which entails reconnaissance survey to identify geological indicators of mineralisation, and the application of geophysical data (gravity and resistivity survey) and remote sensing investigations to delineate structures that serve as conduits for mineral emplacement and to map hydrothermal alteration zones.

By combining gravity data and remote sensing with field observations, this study provides a robust characterization of lithological variations and structural elements within the Asa area, contributing to the broader understanding of its geological evolution and mineral potential. This work also provides a concise geochemical evaluation of mineralisation potential to ascertain the presence of viable ore deposits in the migmatite gneiss complex. Afterwards, the depth and thickness of target zones were defined using the resistivity method. The prospecting and exploration activities focus mainly on the search for precious minerals and metals, e.g. Au, Ag, Cu, Li, nickel and Co.

2. Geology

The geology of the study area is characterized by its location within the Nigerian Basement Complex, particularly the schist belts of southwestern Nigeria. Kwara State is located in the Nigerian Schist Belt between the Pharusian Belt in Northwest Africa and the Borborema Province of Brazil in South America. The mineralisation controls comprise N–S transcontinental faults related to the Pan-African orogeny (600 Ma) that was accompanied by widespread intrusion of granitoids whose late-phase is enriched in pegmatites that host the cassiterite, columbite, tantalite, rare-earth metals and the gemstones (*Ramadan and Abdel Fattah, 2010*). The Pan African event brought about regional metamorphism, a generally N–S foliation trend and the emplacement of granitoids in the region (*Turner, 1983*). A continent-

continent collision-type orogeny has been suggested by *Wright et al. (1985)* which entails an eastward dipping subduction zone where the West African Craton dips beneath the Pan-African region. The continental collision was accompanied by deformation and metamorphism around 660 Ma ago resulting in crustal thickening in the Nigerian region.

Several studies have investigated the gold mineralisation and the host rocks in Nigeria e.g., *Woakes and Bafor (1984)* and *Garba (2003)*. Gold mineralisation is present in alluvial and eluvial placers and primary veins from several parts of supracrustal (schist) belts in the western part of Nigeria prominent of which are those found in Maru, Anka, Malele, Tsohon Birnin Gwari – Kwaga, Gurmmana, Bin Yauri, Okolom – Dogondaji and Iperindo areas (*Garba 2003*). All these areas are spatially related to the two

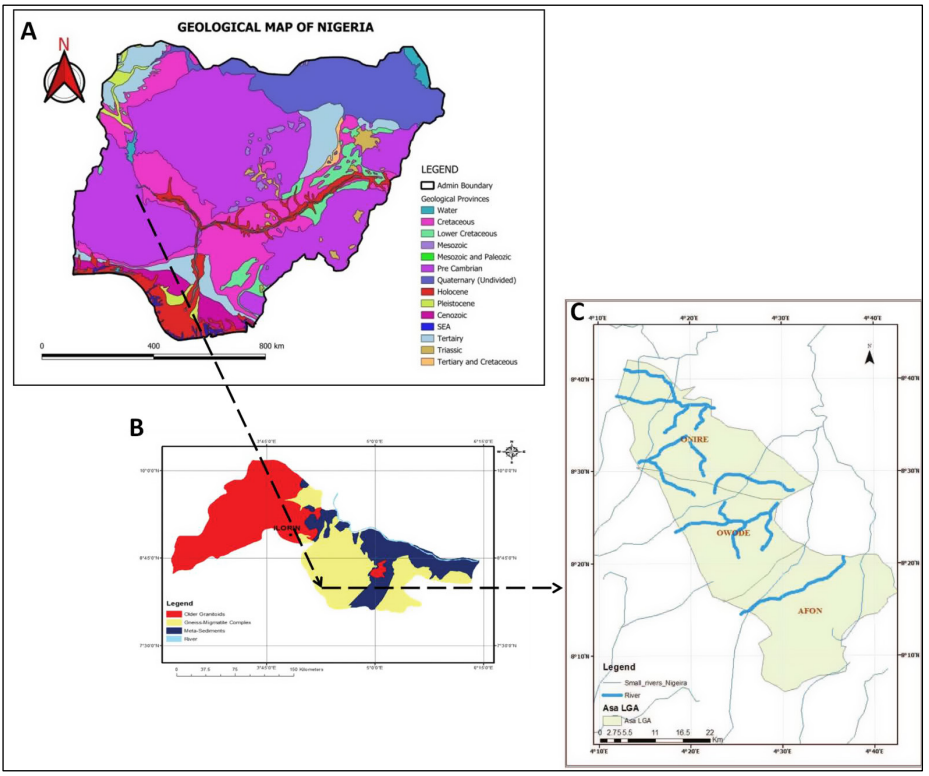

Fig. 1. Map of Nigeria showing inset images of Kwara and Asa local government area (after *Dada and Ajadi, 2018*).

fault systems in the region. The gold-bearing veins, reefs and stringers are often localized by brittle and ductile fault structures or planes of schistosity that traverse schists, quartzites, gneisses and contact aureoles of granitoid masses (*Garba 2003*).

3. Methodology

As shown in Figure 1, the study area, Bielesin, Asa lies in west central Nigeria and is bounded by latitudes $8^\circ\,20'$ N to $8^\circ\,40'$ N and longitudes $4^\circ\,20'$ E to $5^\circ\,00'$ E. A methodological framework was developed to investigate lithological and structural changes in selected parts of Asa Area, Kwara State, using integrated analysis of geophysical survey (gravity data, and electrical resistivity), remote sensing (Landsat imaging), XRF, and field work. This way, geological features and anomalies indicative of lithological variations and structural complexities within the study area were identified. The research approach includes a number of steps as outlined as follows:

a) Firstly, gravity data analysis was conducted to determine geophysical anomalies and structural configurations over the Asa area.

b) Remote sensing data was analysed over the Asa area to directly determine potential hydrothermal deposits and locations of possible mineral enrichments.

c) Afterwards, actual field mapping activities were performed in some of the potential mineralisation areas, delineated in the gravity and remote sensing maps, to obtain crucial ground truth information. This was also done to validate the gravity data and remote sensing-based analyses and offer insights into the geological context of observed anomalies.

d) The observed anomalies, i.e., pegmatite and quartz veins, were sampled. The samples were then subjected to XRF trace geochemical analysis.

e) Subsequently, a pegmatite vein that could serve a potential structure for the enrichment of Au, Ag, Cu and base metals was identified based on the geochemical data and structural configuration. The overburden over the pegmatite vein was first excavated. The pegmatite bearing rock was then trenched and blasted to obtain fresh samples.

f) Vertical electrical sounding was then deployed to determine the thickness of the pegmatite.

3.1. Gravity data

High-resolution gravity data were acquired from the International Gravity Bureau, an International Association of Geodesy (IAG). The maps were then processed. The raw gravity data was corrected for systematic errors, such as tidal effects and instrument drift, using established correction models and algorithms to guarantee its accuracy and suitability for analysis. This was followed by differentiation of the effect of shallow anomaly sources from that of deep-seated anomaly sources in order to produce both residual and regional anomaly fields. This entailed deriving the residual anomaly grids from total field using the filter tool of the Grid and Image tools of the software. Filtering algorithms are applied to potential field data to enhance anomalies from a certain set of geologic sources relative to anomalies due to other geologic sources. The various filtering techniques are explained in the underlying subsections.

3.1.1. Derivatives

Derivatives help to map the source edges and enhance structural features (*Paterson and Reeves, 1985*). This includes first and second vertical derivatives, and horizontal derivative. Analysis of gravity data using the first vertical derivative and horizontal derivative techniques is performed to determine geological feature anomalies to detect structural or lithological contrasts and fault types and the continuity of such subsurface geological structures (*Daud et al., 2019*). The First Vertical and tilt derivations were conducted using the Step by Step Filter to accentuate shallow geological features and delineate lithological and structural boundaries. Lineaments were subsequently extracted from the Residual Bouguer anomaly map by means of the CET analysis tool to extract the ridge/valley structures in the region. The lineaments were then superimposed on the Horizontal Derivative maps through application of the line path on the map tools to directly correlate the acquired features with their respective derived sources.

a. First vertical derivatives (VDR)

Shallow anomalies or bodies are enhanced by vertical derivatives (*Fedi and Florio, 2002; Pham, 2025*). The first vertical derivative sharpens up anomalies over bodies and tends to reduce anomaly complexity, thereby allowing

a clear imaging of the causative structures (*Cooper and Cowan, 2004*). The transformation can be noisy since it will amplify short wavelength noise, that is, clearly delineate areas of different data resolution in the grid. The VDR is given by Eq. (1) below:

$$\mathrm{VDR} = \frac{\partial \varphi}{\partial z}\,. \tag{1}$$

b. Horizontal derivative (HDR)

The horizontal derivative (HDR) method is extensively used to delineate the edges of gravity data (*Cordell and Grauch, 1985*). This enhancement is also designed to look at fault and contact features. Maxima in the mapped enhancement indicate source edges. It is complementary to the filtered and first vertical derivative enhancements above. It usually produces a more exact location for faults than the first vertical derivative. The HDR method also has a characteristic to locate density contrast boundaries from gravity data (*Fedi and Florio, 2001*) and can delineate shallow and deep gravity sources. Maxima in the HDR indicate the location of faults or contacts. The equation (Eq. 2) of the HDR is given by *Cordell and Grauch (1985)* as:

$$\mathrm{HDR} = \sqrt{\left(\frac{\partial \varphi}{\partial x}\right)^2 + \left(\frac{\partial \varphi}{\partial y}\right)^2}\,, \tag{2}$$

where φ is the potential field anomaly.

c. Tilt angle (TDR)

An alternative approach to the conventional phase filter is the tilt angle (*Miller and Singh, 1994*). TDR is used to map shallow basement structures and mineral exploration targets. The tilt filter is utilised for enhancing features and causative body edge detection in potential field images. This edge filter is defined as (Eq. 3):

$$\mathrm{TDR} = \tan^{-1}\left[\frac{\mathrm{VDR}}{\mathrm{HDR}}\right]. \tag{3}$$

3.1.2. Analytical signal

Analytical signal (AS) is used to identify and map the boundaries of different geological features it is also known as total gradient and is defined as the

square root of sum of vertical derivatives for total gravity field anomaly in the $x, y$and$z$ directions (*Thurston and Smith, 1997*). The amplitude of the analytic signal in 3D is expressed by Eq. (5) below:

$$\mathrm{AS} = \sqrt{\left(\frac{\partial \varphi}{\partial \mathrm{x}}\right)^2 + \left(\frac{\partial \varphi}{\partial \mathrm{y}}\right)^2 + \left(\frac{\partial \varphi}{\partial \mathrm{z}}\right)^2}. \tag{4}$$

Thurston and Smith (1997) also define the local wave number k (in radian per ground unit) for this analytical signal to be (Eq. 5):

$$k = 2\pi f_0\,, \tag{5}$$

where f_0 is the cycles unit and k is the wave number in radian per gram unit.

3.1.3. Euler deconvolution

Euler deconvolution maps were produced from the Bouguer gravity data. Three-dimensional (x, y, and z) vertical derivatives were employed to determine the Euler depths. Thus, the Euler approach displays the depths of shallow magnetic anomalies for various structural indices. The Euler 3D tool was used to calculate Euler depths. The standard Euler 3D method is based on Euler's consistency equation which relates the potential field and its gradient components to the source location, with the degree of homogeneity η which may be interpreted as a structural index, SI (*Thompson, 1982*). The SI is an exponential factor corresponding to the rate at which the field falls off with distance, for a source of a given geometry. The Standard 3D form of Euler's equation (*Reid et al., 1990; Pham et al., 2024*) is expressed by Eq. (6) below:

$$(x - x_0)\frac{\partial \varphi}{\partial x} + (y - y_0)\frac{\partial \varphi}{\partial y} + (z - z_0)\frac{\partial \varphi}{\partial z} = \eta\,(B - \varphi)\,, \tag{6}$$

where $\frac{\partial \varphi}{\partial x}, \frac{\partial \varphi}{\partial y}, \frac{\partial \varphi}{\partial z}$ are the derivatives of the potential field φ measured at (x, y, z), which are the coordinates of a measuring point; (x_0, y_0, z_0) represent the coordinates of the source location whose total field is detected at x, y, and z; B denotes a base level, and η symbolizes the structural index (SI).

The SI value depends on the type of source body one is investigating (*Whitehead and Musselman, 2005*). For gravity SI = 0 for thin sheet edge,

thin sill, thin dyke, $\eta = 1$ for line, cylinder, thin bed fault, $\eta = 2$ for point, sphere (*Reid et al., 2014; Moghaddam et al., 2015*). A maximum allowable depth of 4500 metres was provided, with a 10% depth tolerance.

3.1.4. Source parameter imaging (SPI) technique (Local Wavenumber Technique)

Understanding each element that characterizes the sources of the anomalies is requisite for the interpretation of gravity anomalies. Source parameter imaging (SPI), which is based on the Euler deconvolution method, is a significant technique commonly used to provide information about the location, depth and geometry of the subsurface sources of anomalies (structures and mineral deposits) (*Smith et al., 1998*). In this method developed by *Thurston and Smith (1997)*, also referred to as local wavenumber technique, all the parameters that constitute the source, including depth, dip and density contrast are calculated from the complex analytical signal. *Fairhead et al. (2004)* related the source depth to the local wavenumber (k) of the magnetic field which can be derived from the calculated total horizontal and vertical gradients of the RTE grid. The function utilised is the local wavenumber (*Reid et al., 2014*), which is expressed by Eq. (7) below:

$$k(x,y) = \frac{\dfrac{\partial^2\varphi}{\partial x\partial y}\dfrac{\partial\varphi}{\partial x} + \dfrac{\partial^2\varphi}{\partial y\partial z}\dfrac{\partial\varphi}{\partial y} + \dfrac{\partial^2\varphi}{\partial^2 z}\dfrac{\partial\varphi}{\partial z}}{\left(\dfrac{\partial\varphi}{\partial x}\right)^2 + \left(\dfrac{\partial\varphi}{\partial y}\right)^2 + \left(\dfrac{\partial\varphi}{\partial z}\right)^2}. \tag{7}$$

3.2. Landsat imaging: ratio technique

ArcGIS software was used to process Landsat images and band ratio maps of the study area. Band ratio maps were utilised to efficiently visualize spectral variations, which enable delineation of hydrothermal alteration and potential mineralisation zones. The ratios amplify some slight disparities in spectral response and allow for the differentiation of materials based on their varying distinctive spectra. A ratio is generated through the division of brightness values, pixel by pixel, of one band by another. Although 3/1, 5/7, and 5/4 are frequently used in false colour composite images generated from Landsat satellite data for mapping hydrothermal alteration zones

(*Imbroane et al., 2007; Andongma et al., 2021*), this study chose bands 4/2, 6/5 and 6/7, which represent ferric iron, ferrous iron, and hydroxyl bearing clay minerals, respectively. These combinations were selected due to their sensitivity to lithologic variables (*Ousmanou et al., 2024*). The 4/2 band combination indicates the presence of ferric minerals (iron oxides), which include hematite, goethite and limonite that are primarily present in weathered profiles and overburden (*Ali and Pour, 2014; Ousmanou et al., 2024*). The band ratio 6/5 map shows the concentrations of ferrous minerals that include pyrite and pyrrhotite, usually contained in altered rocks and crystalline rocks rich with mafic minerals, while the band ratio 6/7 reflects hydroxyl (OH)-bearing minerals (i.e. clay minerals such as kaolinite)often associated with hydrothermal alteration and weathering processes (*Ousmanou et al., 2024*).

The methodology of mineral deposit detection using satellite imaging comprises two steps: preliminary analysis to determine potential points of interest (POIs), which could include mineral deposits, and high-resolution analysis of the area around each POI. The preliminary analysis entailed the detection and cropping of area of interest within the image. This also involved the application of certain geometric corrections on the area, like rotation for enhanced visualization, and reduction of spatial resolution. The POI detection method works on 2×2 matrix of neighbouring pixels. The POIs are categorized as mineral deposits based on mineral operators. The second step classifies the area contiguous to each POI through application of a similar set of the mineral operators. The mineral operators are derived by mapping the ratio of different bands like B3/B1, B5/B7 and B5/B4 to Red, Green and Blue channels in the visible spectrum. The resulting image shows the areas that are hydrothermally-altered, which are potential hosts of some mineral deposits.

3.2.1. Procedures

Landsat 8 data was downloaded from USGS Earth Explorer at less than 10% cloud cover. The data was imported into Geomatica software. Image filtering was done using the Sobel to enhance lineaments after which the Canny edge detection algorithm was employed to outline the lineaments. A lineament enhancement filter was used to highlight linear features. The extracted lineaments were then imported into ArcGIS in vector format which

was plotted as a map. A line density map was plotted for the lineaments using the line density tool of the spatial analysis tools.

3.2.2. Method for elevation

The Digital Elevation Model was downloaded from USGS Earth Explorer at less than 10% cloud cover. The EM was then imported into the ArcMap. The Extract tool from the Raster in the spatial analysis tools was used to extract the elevation. The extracted elevation was classified with colours for visualization and plotted as a map.

3.3. Field study

This comprised reconnaissance and detailed (follow-up) studies, where structures that serve as hosts and geological indicators of potential mineralisation were identified, observed and analysed. The field study specifically covers the Bielesin area in Asa. This area was specifically chosen based on the potential mineralisation areas delineated from the Bouguer anomaly map and remote sensing data. The area has a high prevalence of outcrops. Samples taken from streams, pegmatite and quartz veins were compositionally analysed to determine the presence of enriched metals. The potential target pegmatite that showed high concentration of valuable elements was subjected to excavation, trenching and blasting to obtain fresh samples.

3.4. Chemical composition

The trace elemental composition of the samples was determined using Energy Dispersive X-ray Florescence (EDXRF) spectrometer (Rigaku NEX DE EDXRF spectrometer) equipped with a 15-place sample changer with spin function using slow and steady spinning mode. Mass Attenuation Coefficient (MAC) calibration is carried out through measurement of a set of standards (GSR 10, BIR-1a, PM-S, GMO-02, AGV-2, GSR-09, AN-G, GSR-08, GSR-02, UB-N, GSR-04) to obtain a graph showing the Compton intensity or Compton/Rayleigh ratio versus mass attenuation coefficient. Six standards (GSR 01, GSR 04, GSR 06, N3 ICP, NOD P1, GBM309-16) with a concentration range of 20 – 106,947 μg/g are used for Compton calibration, while 16 standards (GSR 04, AN-G, PN-S, BIR-1a, GSR 02,

GSR 09, AGV-2, GMO-02, GSR10, GSR 03, GSR 08, AC-E, NIST 2782, NIST 2781, NOD P-1, UB-N) covering a concentration range between 20 – 1600 μg/g are utilised for fundamental parameter calibration.

The rock samples were prepared by crushing them using a pulveriser into a homogenous mix of about 100 – 200 mesh size. 5 g of each sample was then put into 32 mm sample cups with a polypropylene X-ray film thickness of 4 μm. Pellets of the samples were obtained via hydraulic pressing. Sample heights were measured in millimetres and sample cups were capped. The samples were then analysed.

3.5. Resistivity data

After delineating the potential areas of mineralisation from the gravity and lineament maps, a resistivity survey was conducted on the target mineralisation areas to determine the thickness of overburden and depth to possible intrusive rocks. Six 200 m resistivity profiles were obtained across the study area. Five shorter profiles were obtained at a precise point to determine continuity in subsurface lithology. The conventional Schlumberger array was utilised for vertical electrical sounding (VES) using the Ohmega resistivity meter. The acquired VES resistivity data was processed using the IPI2WIN software, which is capable of refining the interpretation and extracted true resistivity along with layer parameters (*Vander Velpen, 2004*). Geoelectric sections were then generated from the VES curves.

4. Results and discussion

4.1. Gravity anomalies

Gravity anomalies observed in the study area provide valuable insights into subsurface geological structures and lithological variations, despite the predominantly covered environment. Although the study area is covered by overburden, gravity anomalies serve as effective indicators of subsurface geological structures. Variations in gravity values reflect differences in rock types, densities, composition and thicknesses, aiding in the identification of concealed lithological units and structural features such as faults, folds, and intrusions. Figure 2a presents the Bouguer gravity anomaly map of the area, showing variations in subsurface formation density, after correction for

latitude, elevation and terrain effects. As observed, gravity is depicted to vary across different areas of the map, possibly due to large-scale structural variations. The colour legend bar identifies regions of gravity high (red and pinks) analogous to region with high density contrast beneath the subsurface; intermediate values (green and yellow) and gravity lows (blue colour) correspond to regions of low density contrast. The high gravity (positive) anomaly zones are indicative of denser rocks, or may be due to the presence of shallow intrusions or thin sedimentary cover overlying the crystalline basement rocks. In contrast, the negative and low gravity anomalies can be attributed to basement lows and the presence of less dense bodies or intrusions, faults or fractures with low density fillings, and thick sedimentary sections or overburden. The discernible irregular anomaly patterns suggest complex geological structures or multiple overlying features.

Afterwards, the residual gravity map was determined by removing the regional trend or background gravity field, in order to show the more localized and discrete variations in gravity. The residual anomaly map (Fig. 2b) also shows lateral changes in the earth's gravity field with a maximum anomaly value of 5.58 mGal at the northwestern and western parts and minimum anomaly value of about −8.83 mGal in the eastern and southeastern parts of the study area. Similar to the Bouguer anomaly map, the residual gravity map shows low gravity readings in the western flank of the area. The eastern part of the map also shows low gravity reading areas. The negative or low anomalies suggest the presence of low-density subsurface structures and low density rocks. The residual anomaly map tentatively shows three zones: the overcompensated zone with negative anomalies resulting from the presence of sediments (*Epuh and Joshua, 2017*) in the form of overburden in the eastern and western parts of the area; second zone characterized by zero anomaly values indicating a zone of equilibrium, and the undercompensated zone comprising positive anomaly values in the northern and southern parts indicating the crystalline basement rocks.

Subsequently, filtering techniques were applied to enhance the images. The first vertical derivative map (Fig. 2c) displays structures that can be related to the geology of the area. It highlights the edges and boundaries of subsurface structures. The map shows a sequence of high (positive anomalies) and low (negative anomalies) density areas, indicating basement highs and lows (thick overburden), respectively. The lineaments trend along ar-

eas of density contrasts, marking zones of potent mineralisation. Similar to the residual map, the Eastern and southeastern parts of the study area show low density zones demarcated by basement highs. The circular or oval shaped anomalies with positive density contrasts may indicate intrusions.

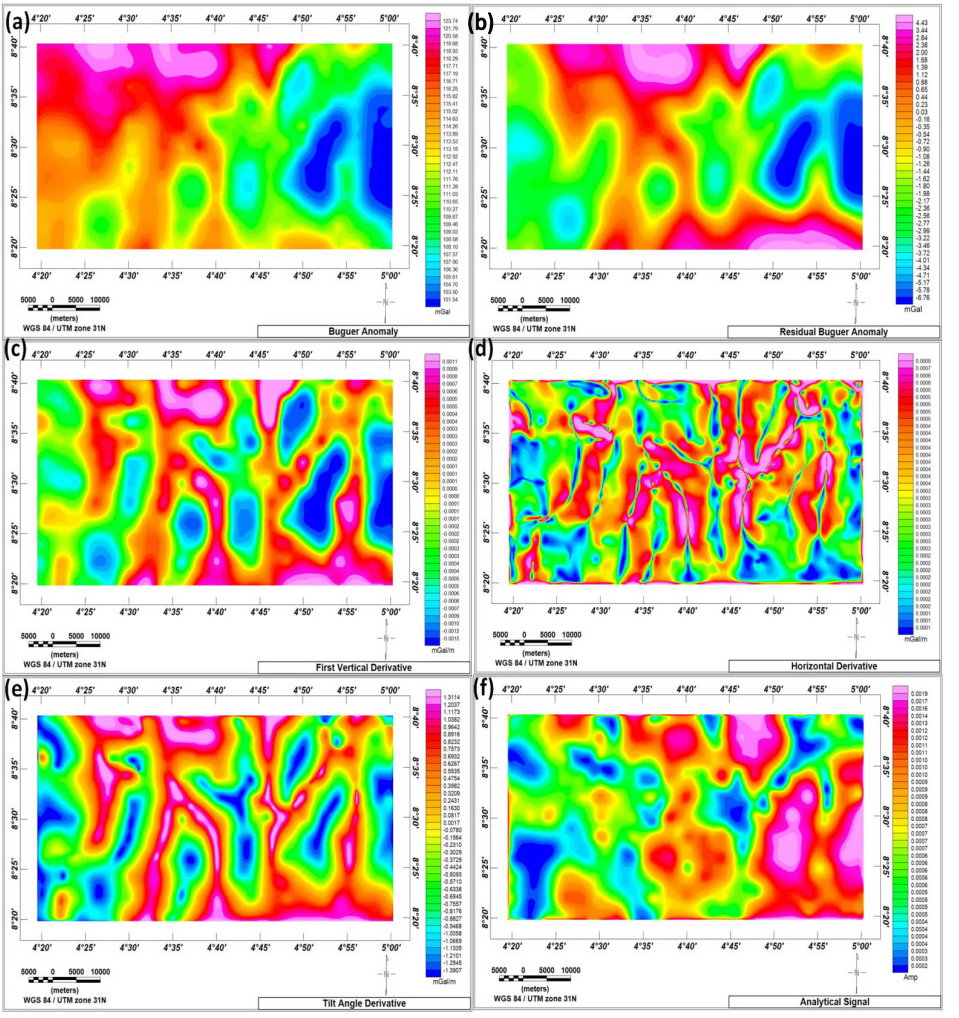

Fig. 2. Lineaments superimposed on (a) Bouguer anomaly map, (b) Residual anomaly map, (c) First vertical derivative (VDR) map, (d) Horizontal derivative (HDR) map, I Tilt angle (TDR) map, (f) Analytical Signal (AS) map.

The horizontal derivative (HDR) map is presented in Fig. 2d, which employs spatial variations in the gravitational field to infer subsurface structures and density distributions. The HDR gravity map provides more enhanced edge detection, and shows the directions of the delineated subsurface features, unlike the first vertical derivative (VDR) map. As observed, the positive and negative anomalies indicate areas of high and low densities, respectively.

The analytical signal (AS) map (Fig. 2f) shows the spatial distribution of gravity anomalies based on amplitude and wavelength. The analytical signal values vary from 0.0003 to 0.0032 Amp where the map indicates the direct source of the anomaly. The pink portion shows near surface or high contrast between rocks of differing geologic composition in the study area, the blue portion might be a sedimentary cover or a stream, while the pink colour suggests an intrusion or lithological change. The lithological variations are visibly represented by gravity signal discontinuities. However, searching for both lithological and structural discontinuities at the same time is a complicated process using AS gravity map; hence the tilt angle derivative (TDR) technique of interpretation was employed (Fig. 2e). Since the TDR map (Fig. 2e) can simultaneously increase both short and long wavelength anomalies, it offers more details compared to both residual (Fig. 2a) and AS (Fig. 2f) maps. Based on a colour scale, the legend aids recognition of the edge (boundaries) of source bodies such that the source body, edge, and external source bodies are denoted by pink, red, yellow, green, and blue colours, respectively. The peaks of gravity anomalies are more conspicuous and sharper, while the signal for weak anomalies is made broader by TDR, which is a valuable technique for delineating deep sources. A maxima in the AS (Fig. 2f) and a minimum in the TDR (Fig. 2e) map characterize the region at the eastern part of the study area. Nonetheless, TDR is obviously more capable of enhancing the delineation of both deep and shallow seated bodies compared to AS. NE–SW, E–W, and NW–SE striking faults, which represent the direction of boundary faults, are depicted at their respective locations.

The lineaments in the area were extracted, denoting zones of structural density and indicating underlying geological structures (i.e. fractures, faults) that may serve as host for hydrothermal veins and pegmatite mineralisation, making them targets for the exploration of minerals. The high structural density indicates potential mineralisation zones, reflecting the significance

of lineaments density map to detect potential mineralisation zones and the structures controlling mineralisation. Thus, a lineament map (Fig. 3a) was obtained, which is based on the lineament detection from the gravity data. The extracted lineaments were superimposed on the TDR map (Fig. 3b) to

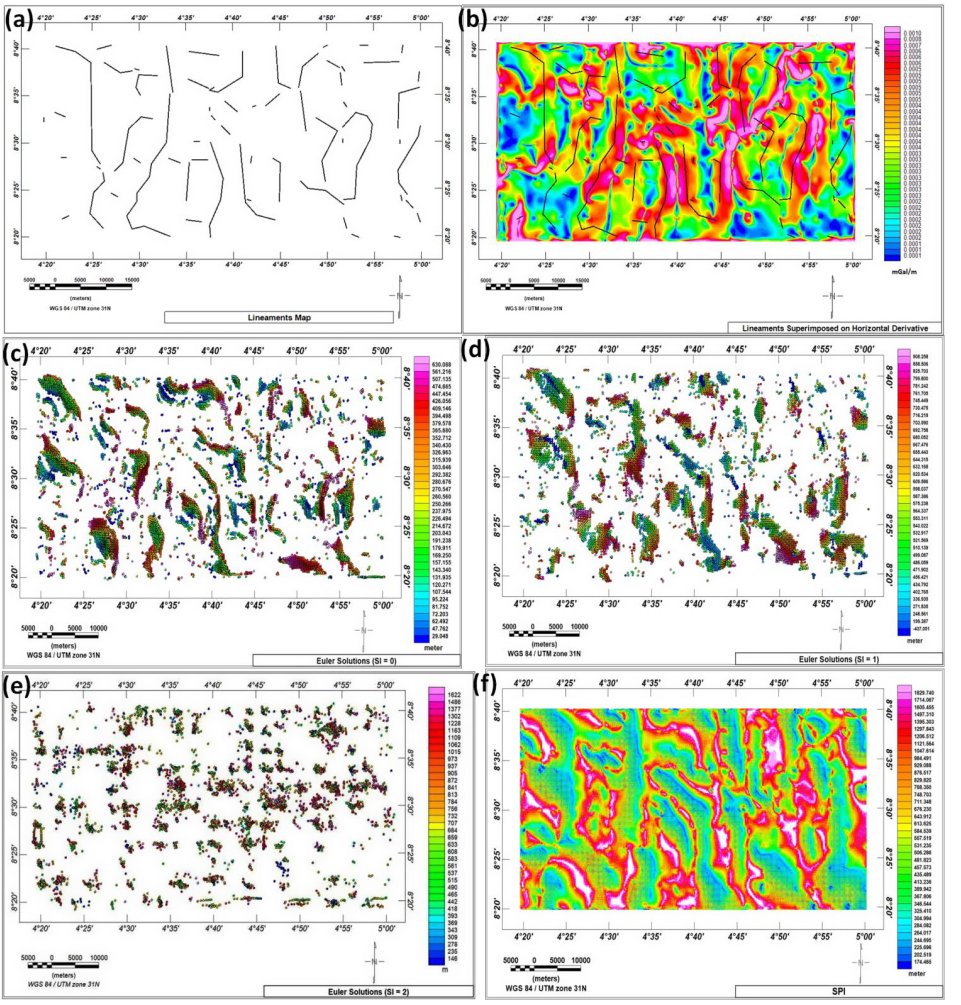

Fig. 3. (a) Lineaments map, (b) Lineaments superimposed on TDR map, (c) Euler Solution map for SI=0, (d) Euler Solution map for SI=1, and (e) Solution map for SI=2, and (f) SPI map.

match structural trends with the edges of anomalies. As observed, the map displays zones of high structural complexity represented by a major (north-south) NS trend along with less common NNW, NNE, NS, and WE trends. Extended lineaments are majorly present within the negative anomaly zone. The Euler solution maps (Fig. 3d, 3e, and 3f) were used to estimate the depth and location of the subsurface structures. SI = 0, 1 and 2 denote thin sheet edge, thin sill, thin dyke; thin bed fault, and sphere, respectively. The estimated depths of the thin sills and dykes (horizontal contacts for subsurface structures) (Fig. 3d), which could be faults and intrusions, ranged from 29 to 630 m. For the thin bed faults, tops of vertical structures, the depths vary from approximately −430 (outcrops) to 908 m (Fig. 3e). For the deep-seated, spherical shaped anomalies (Fig. 3f), the depths vary between 146 and 1622 m. The SPI map provided depth estimates of anomaly sources. As observed in Fig. 3f, the depths of density contrast range from 174 to 1830 m.

4.2. Remote sensing imagery data: Landsat imaging (band ratio maps)

The band ratio technique involves enhancement of the spectral properties of alteration minerals to recognise the alteration regions. The concentration of hydrothermal alteration minerals is significantly related to the occurrence of mineralised alteration zones, particularly gold mineralisation, which are frequently correlated with highly-sheared areas (*Pour et al., 2019*). The target location is within the Basement Complex of Asa area of Kwara State. The processing covers the multispectral bands 1, 3, 4, 5 and 7 of the Landsat ETM+ image of this geographical area. Figure 4a presents the 4/2 band combination, where the red denotes the presence of ferric minerals (iron oxides), which include hematite, goethite and limonite. These minerals are typically present in sedimentary and crystalline rocks as well as soils resulting from intense oxidation and hydrolysis of the initial crystalline rocks. Dark blue, dark green, and bright green colours represent water bodies, vegetation cover, and rock alteration, respectively. Based on the high concentration of ferric minerals, the highlighted red-coloured areas, in the western part of the map, can be categorized as possible mineral deposits. Figure 4b presents the band ratio 6/5 map, which shows the concentration variation of ferrous minerals that include pyrite and pyrrhotite. These

minerals are usually contained in igneous and metamorphic rocks rich with mafic minerals. The yellow-coloured areas in the 6/5 map denote very high concentration of ferrous minerals, which is consistent with the band ratio 4/2 map.

As shown in Fig. 4c, the band ratio 6/7 clearly reflected the hydroxyl (OH)-bearing minerals (clay minerals; e.g., kaolinite, montmorillonite, alunite, etc.) in bright tones depicted by yellow and red colours. The blue-coloured areas, mostly in the western sector of the study area, are very low in hydroxyl bearing minerals. This suggests the primary minerals in these areas were weathered into the clays/hydroxyl minerals, which were then dispersed to the south-eastern parts of the study area. The altered spots of white tones correspond to elevated responses in the band ratio (*Gabr et al., 2022*).

The combination of lineament map and alteration zones allows the prediction and mapping areas of potential high mineral resources (*Eldosouky*

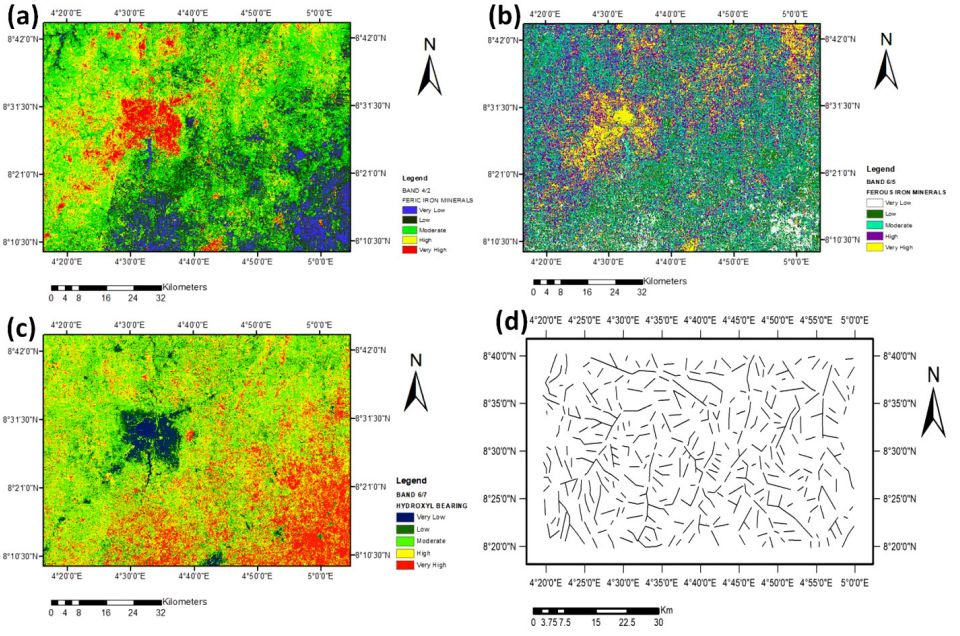

Fig. 4. Landsat image ratios for (a) 4/2 band, (b) 6/5 band, and (c) 6/7 band, (d) surface lineations extracted from the satellite data.

et al., 2017). Thus, a lineament map (Fig. 4d), developed on the basis of lineament detection from remote sensing data, was also produced, which showed zones of intense structural complexity indicated by a major NE–SW trend along with less common NNE, and NW trends. These lineaments likely indicate the streams, gullies, narrow depressions and erosion surfaces. The western part of the map is identified a potential area of high mineralisation.

4.3. Field geology – ground-truthing

Given that quantitative interpretation is normally dependent on geological interpretations, it is hardly ever original or precise. Hence, to obtain interpretable information, there is need for adequate understanding of geology. The field mapping activities were carried out within the Bielesin area of Asa region to ascertain the geology based on the gravity and remote sensing data, focusing on identifying lithological units, structural elements, and mineral occurrences. Areas identified as potential locations of mineral deposits on the maps ($4^\circ\,22''$ E; $8^\circ\,27''$ N) were then scrutinized. Focus was given to the Bilesen village in Asa local government area, based on the basement highs demarcated in the western flank of the gravity map and Landsat images. The study area evidently consists of rocks characteristic of the basement complex of Nigeria (Fig. 5a), with metamorphic structures that are suggestive of the varying levels of deformation they have been subjected to. The outcrops mostly occur as broad low lying exposures and occasionally as low ridges. These rocks include the migmatitic gneiss, alkali granite, pegmatite/aplite and vein quartz.

Migmatite gneiss, shown in Fig. 5 underlay over 50% of the study area. The gneisses comprise biotite gneiss, granite gneiss and augen gneiss with textures of medium to coarse-grained. The combination of these gneisses along with other granitic rocks on a single outcrop produces the migmatites. In some cases, the different gneissic units outcrop as discrete mappable bodies in the forms of low lying exposures and low ridges, as observed in Fig. 5. The migmatitic structures identified include schollen (Fig. 5c) and stromatic (Fig. 5d,e) types. The flaggy biotite gneiss was also identified (Fig. 5d).

The observed folded gneissose foliation, schollen and stromatic folds, pegmatites and quartzo-feldspathic veins, and lenses of biotite are indicative of

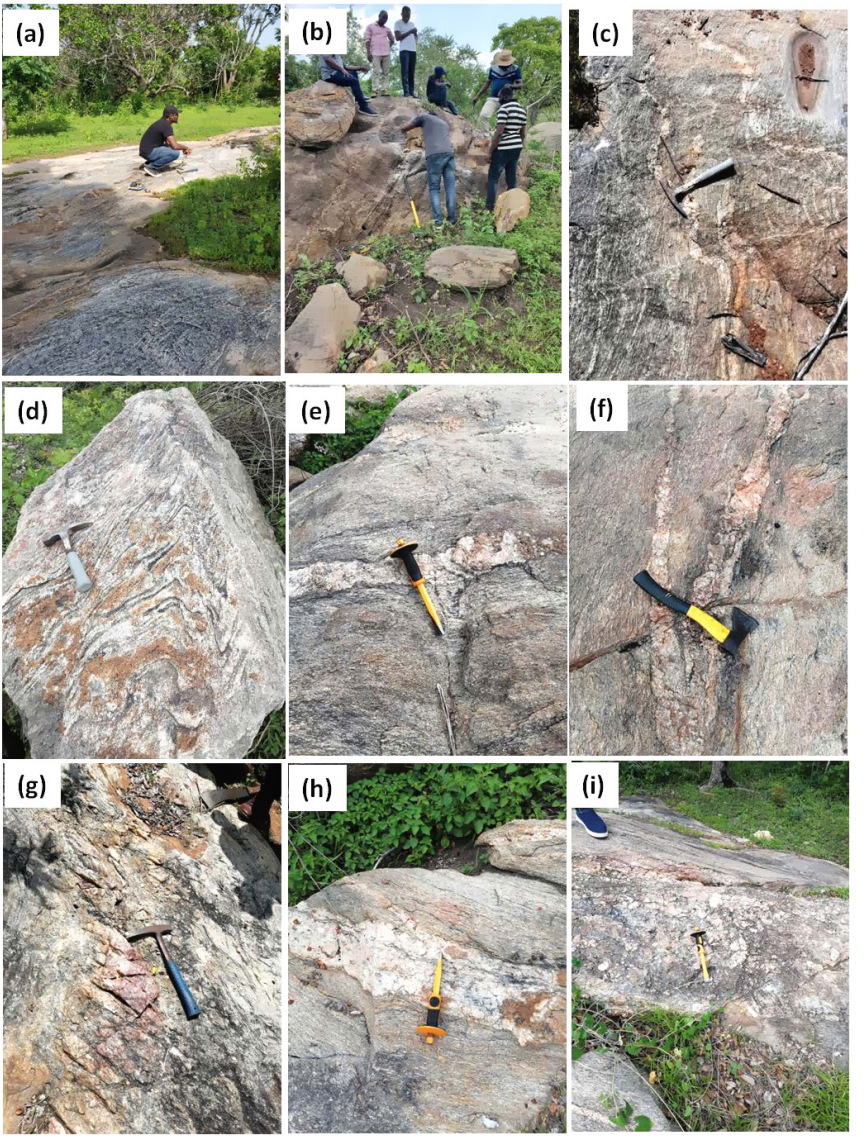

Fig. 5. Outcrops mostly occurring as (a) broad low lying exposures, and (b) low ridges, (c) section of an outcrop of migmatitic gneiss showing schollen structure, (d) flaggy biotite gneiss (d) concordant and (e) discordant alignment of the stromatic structure in migmatite gneiss (g) fractured pegmatite intrusion in the gneiss structure (h) quartz veins (1) thick weathered pegmatite body intruding the migmatite gneiss.

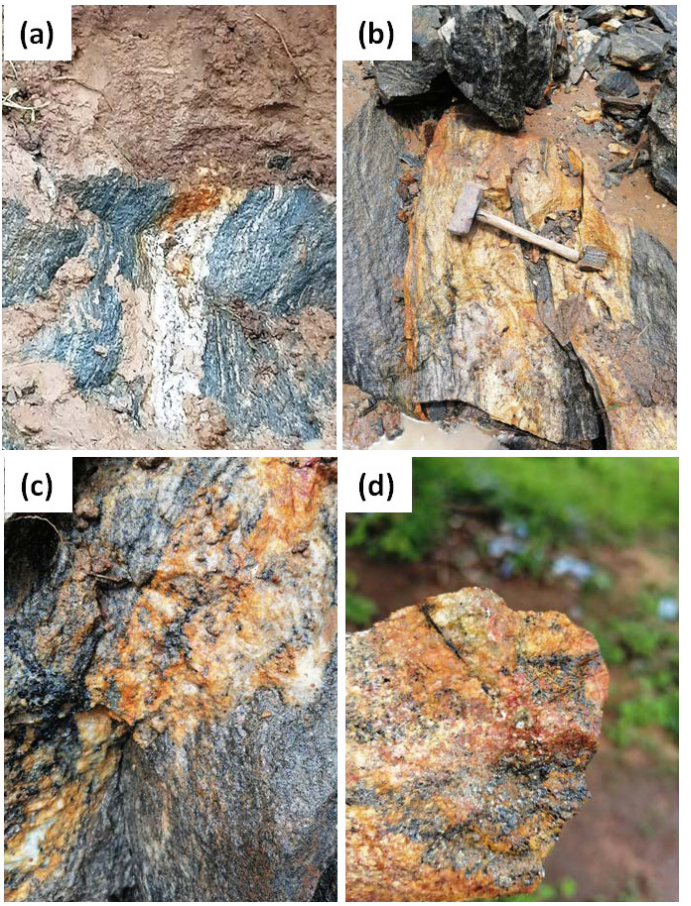

Fig. 6. (a) Exposed rock surface after removal of overburden, (b) leucosome in the gneissic rock, (c) (d) closer look of the leucosome showing the accessory minerals.

the partial melting of pre-existing rock i.e., anatectic melting *(Obiora and Ukaegbu, 2009*). This anatexis allows for the enrichment and concentration of valuable and critical elements in the crustal melt, leading to the formation of pegmatites (*Knoll et al, 2023*). Thus, the pegmatites identified in this study area can be regarded as anatectic type. The anatexis evidently produced both the paleosomes and leucosomes. The palaesome is composed of biotite gneiss (Fig. 5d), whereas the leucosome comprises granitic gneisses, pegmatite (Fig. 5g) and quartz-feldspathic vein (Fig. 5h). The leucosome in

Fig. 7. Pegmatite in migmatite gneiss with arrow indicating the fresh rock sample with matted texture of black dots (tourmaline).

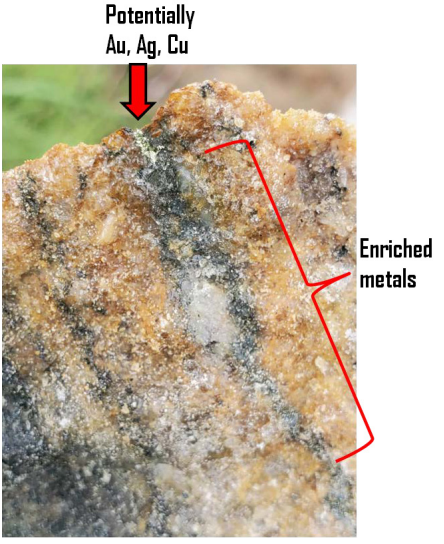

Fig. 8. Closer look at the pegmatite rock sample showing potentially gold (Au), silver (Ag) and copper (Cu).

the gneissic rock, comprising pegmatite and quartzo-feldspathic vein, was then sampled to check for potential enrichment of valuable minerals.

To ensure a good exposure of the outcrop, the overburden was removed (Fig. 6a). A trench was then created, at right angle to the general strike, across the mineralised zone. The exposed rock was then hammered to obtain a fresh surface (Fig. 6b). A closer look of the leucosome sample (Fig. 6c,d) shows the presence of accessory minerals that could include silver and gold. Figure 7 presents the pegmatite sample showing quartz, feldspar, schorl tourmaline and accessory minerals. This sample was obtained following the boring and blasting of pegmatite that is deep within the migmatite gneiss rock. Compositionally, the coarse grained igneous rock comprises light-coloured minerals (quartz, feldspar) and a matted texture of black dots (tourmaline). A closer look at the pegmatite rock sample (Fig. 8) shows the presence of gold (Au), silver (Ag) and copper (Cu).

4.4. Geochemical analysis

Geochemical data analysis is reliable as a reconnaissance and exploitability appraisal tool to complement the geophysical survey, prior to rock surface excavation. A challenge in the discovery of disseminated mineralisation such as gold deposits is the micron size of the fine-grained gold. Since significant amount of gold can be present as discrete grains encased within fine-grained silica, the sampling and geochemical analysis must be accurate to detect all the gold present. The trace elemental compositions of samples from the study area were analysed to determine concentrations of precious elements and their associated metals. Several samples were taken from the stream, pegmatites, quartz veins, and mined pits in the target area. As shown in Table 1, the geochemical analysis showed the presence of Mo, Zr, Sr, U, Rb, Th, Pb, Zn, Cu, Ni, Mn, Fe, Co, Nb and Ti. Cr and V were identified in some samples. These pathfinder elements can be extremely informative about the nature of the gold anomaly. The concentration ranges of the main metals in the samples are Cu (11.3 – 30 ppm), Pb (4.3 – 61.1 ppm) and Ag (0.03 – 0.5 ppm). The relatively high concentrations of Cu, Pb and Ag reflect the abundance of galena and secondary copper minerals in the host migmatite gneiss rock in the area. The base metal content indicates a correlation with the Au mineralisation (hydrothermal alteration). The

concentrations of Au vary from 0.0205 to 3.411 ppm, as shown in Table 1, which confirmed the presence of Au in the area. The pegmatite sample with visible gold particles (Fig. 8) gave an Au value of 3.411 ppm. The Au concentration values of > 2 ppm indicate an average quality grade of gold deposit for the market. However, the Au concentration of < 1 ppm in some of the samples is uneconomic, but is an indication of a good potential for economic gold grade within the mineralisation. As observed in Table 1, the concentrations of strontium, Pb and Zn have average values of value, 160 ppm, 19 ppm, and 74 ppm, which are above the thresholds set for anomalous populations (*Sanusi et al., 2024*).

The Ni concentrations obtained from the whole rock analyses were also utilised to deduce the origin of the mineralising fluids. The geochemical analyses revealed Ni concentration range of 23 to 67 ppm in some of the rock samples, indicating that the mineralising fluids responsible for the quartz-veins are of sedimentary-metamorphic parentage (*Rye and Rye, 1974*). sThis inference is consistent with the geology of the host rock. In addition, the inter-element ratio of specific large ion lithophile elements (LILE) Rb and Sr in the analysed samples were utilised for additional interpretation of the nature of the gold mineralising fluids. The range of Rb/Sr ratio varied from 0.042 to 5.32 ppm. According to *Taylor and McLennan (1985)*, the average crust has inter-element ratios of 0.123 for Rb/Sr. Hence, majority of the samples are characterized by Rb/Sr ratio that is similar to those of average crustal ratios.

The sampled area with the highest concentration (i.e., 3.411 ppm) was then subjected to resistivity survey to determine the potential thickness of the mineralisation. The absence of Au in the stream samples is suggestive of low secondary dispersion halo.

4.5. Depth estimation of mineralisation using resistivity data

Vertical electrical sounding (VES) was conducted in the sampled area with the highest Au concentration (i.e., 3.411 ppm) as shown in Fig. 9. The resistivity data and curves are presented in Figs. 10 and 11, and Table 2. Evaluation of the VES data entails analysing the plot of apparent resistivity against electrode spacing to derive the geoelectric parameters of the explored section, comprising the resistivities and thicknesses of delineated

Table 1. Trace element geochemical analysis of some rock samples from the study area.

Elements	Concentration (ppm)				
	1 Stream sample	**2 Vein**	**3 Pegmatite**	**4 Vein**	**5 Vein: pit sample**
Mo	3.027	2.242	–	3.310	2.343
Zr	105.246	4.761	–	2.653	2.185
Sr	97.587	271.894	5.140	72.635	22.687
U	–	–	–	8.905	3.222
Rb	21.341	59.718	1.755	386.724	14.223
Th	–	–	–	–	2.503
Pb	18.147	20.520	–	67.123	4.045
Au	–	–	3.411	0.0656	–
Se	–	–	–	–	–
As	–	–	–	–	–
Hg	–	–	–	–	–
Zn	79.222	66.972	55.309	175.607	62.914
W	–	–	–	–	–
Cu	–	18.306	11.903	17.694	12.849
Ni	–	46.907	28.425	–	–
Co	–	–	23.047	139.672	–
Fe	37071.109	2459.473	529.437	44521.750	2680.038
Mn	413.490	184.167	107.759	183.337	208.332
Sb	–	–	–	–	–
Sn	–	–	–	–	–
Cd	–	–	–	–	–
Pd	–	–	–	–	–
Ag	–	0.2260	0.1796	–	0.02604
Bal	962346.938	958447.563	994227.000	923132.625	949782.563
Nb	5.002	–	–	3.284	2.415
Bi	–	–	–	–	–
Pt	–	–	–	–	–
Re	–	–	–	–	–
Ta	–	–	–	–	–
Hf	–	–	–	–	–
Cr	–	–	33.539	–	–
V	–	–	–	–	–
Ti	–	–	102.523	447.068	–
Rb/Sr	0.22	0.22	0.34	5.32	0.63

Table 1. Continued from the previous page.

Elements	Concentration (ppm)				
	6 Vein	**7 Stream sample**	**8 Vein**	**9 Vein**	**10 Pegmatite**
Mo	3.910	7.355	3.390	–	–
Zr	4.164	514.168	9.473	18.794	13.605
Sr	16.624	48.149	283.088	233.455	115.510
U	3.458	–	6.001	5.868	–
Rb	6.144	18.949	18.119	76.582	99.339
Th	2.389	–	2.731	2.656	3.075
Pb	4.292	6.975	16.135	16.712	22.110
Au	–	–	2.823	–	0.0205
Se	–	–	–	–	–
As	–	–	–	–	–
Hg	–	–	–	–	–
Zn	85.121	60.947	69.684	78.485	76.992
W	–	–	–	–	–
Cu	21.905	–	28.677	11.277	21.595
Ni	–	–	–	25.749	–
Co	–	116.575	30.519	–	–
Fe	1470.462	33934.328	2136.490	2136.490	1533.463
Mn	154.714	551.321	176.616	176.616	159.180
Sb	–	–	–	–	–
Sn	–	–	–	–	–
Cd	–	–	–	–	–
Pd	–	–	–	–	–
Ag	–	0.2659	0.2492	–	0.4909
Bal	958315.500	954132.313	968135.125	963012.313	943177.875
Nb	3.418	5.687	5.687	7.746	2.663
Bi	–	–	–	–	–
Pt	–	–	–	–	–
Re	–	–	–	–	–
Ta	–	–	–	–	–
Hf	–	–	–	–	–
Cr	21.911	35.592	–	–	–
V	0	51.864	–	43.704	–
Ti	77.931	1365.287	174.339	629.460	–
Rb/Sr	0.37	0.39	0.064	0.33	0.86

Table 1. Continued from the previous page.

Elements	Concentration (ppm)				
	11 Vein	**12 Vein**	**13 Vein**	**14 Vein**	**15 Vein**
Mo	2.043	–	–	–	–
Zr	22.247	–	2.763	3.630	66.779
Sr	83.580	312.421	136.788	288.479	401.711
U	6.424	5.041	–	–	–
Rb	152.542	59.940	46.212	113.362	16.931
Th	9.993	3.064	2.535	–	–
Pb	33.619	20.702	16.226	24.041	13.994
Au	–	0.0422	–	–	0.0286
Se	–	–	–	2.538	–
As	–	–	–	–	–
Hg	–	–	–	–	–
Zn	72.394	57.678	51.653	60.397	62.983
W	–	–	–	–	–
Cu	30.040	22.591	14.356	12.460	12.599
Ni	–	–	46.556	67.183	23.033
Co	–	–	–	34.271	–
Fe	2081.283	1769.436	1521.789	603.413	3023.725
Mn	171.522	166.191	138.931	180.383	147.659
Sb	–	–	–	–	–
Sn	–	–	–	–	–
Cd	–	–	–	–	–
Pd	–	–	–	–	–
Ag	–	–	–	–	0.1589
Bal	951053.655	961825.938	978809.188	950268.188	971703.188
Nb	7.274	–	0	1.897	–
Bi	–	–	0	–	–
Pt	–	–	–	–	–
Re	–	–	–	–	–
Ta	–	–	–	–	–
Hf	–	–	–	–	–
Cr	–	–	–	–	–
V	–	–	53.389	53.389	–
Ti	205.017	205.017	356.289	356.289	–
Rb/Sr	1.83	0.19	0.34	0.39	0.042

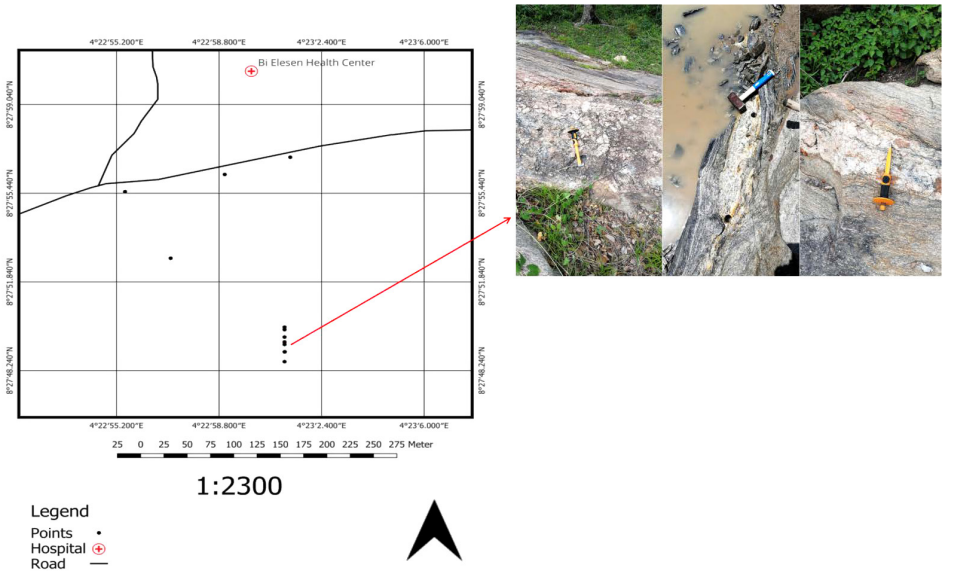

Fig. 9. Map of the delineated area showing the points of resistivity survey lines. The arrow indicates the pegmatite vein that was explored using the resistivity survey.

layers. As observed, the majority curve types delineated from the geoelectric models are H and HA types. With the exception of one sounding, Figure 10 present the VES curves for the Schlumberger surveys, denoting a H type curve, which indicates an initial high resistivity geoelectric layer that represents the crystalline rock, accompanied by a decrease in resistivity that corresponds to a weathered/fractured basement layer that is probably saturated or infilled with less resistive rock materials, and ensuing rise in resistivity that represents the unweathered/fresh basement. The delineated lithologic units corresponding to resistivity values are presented in Table 2. The resistivity of the top crystalline rock layer varies from 643 to 3526 Ω·m and its thickness varies from 0.42 to 2.4 m. The resistivity value of the fractured basement layer ranges from 18.18 to 180 Ω·m, while its thickness varies from 0.793 to 15.4 m. The resistivity of the fresh basement varied from 352 to 35397 Ω·m. Table 2 presents the measured apparent resistivities, thicknesses, depths and lithologies for the various VES sites.

The weathered/fractured layer corresponds to the pegmatite intrusive rock, which is the target of the exploration. The depth and thickness of this

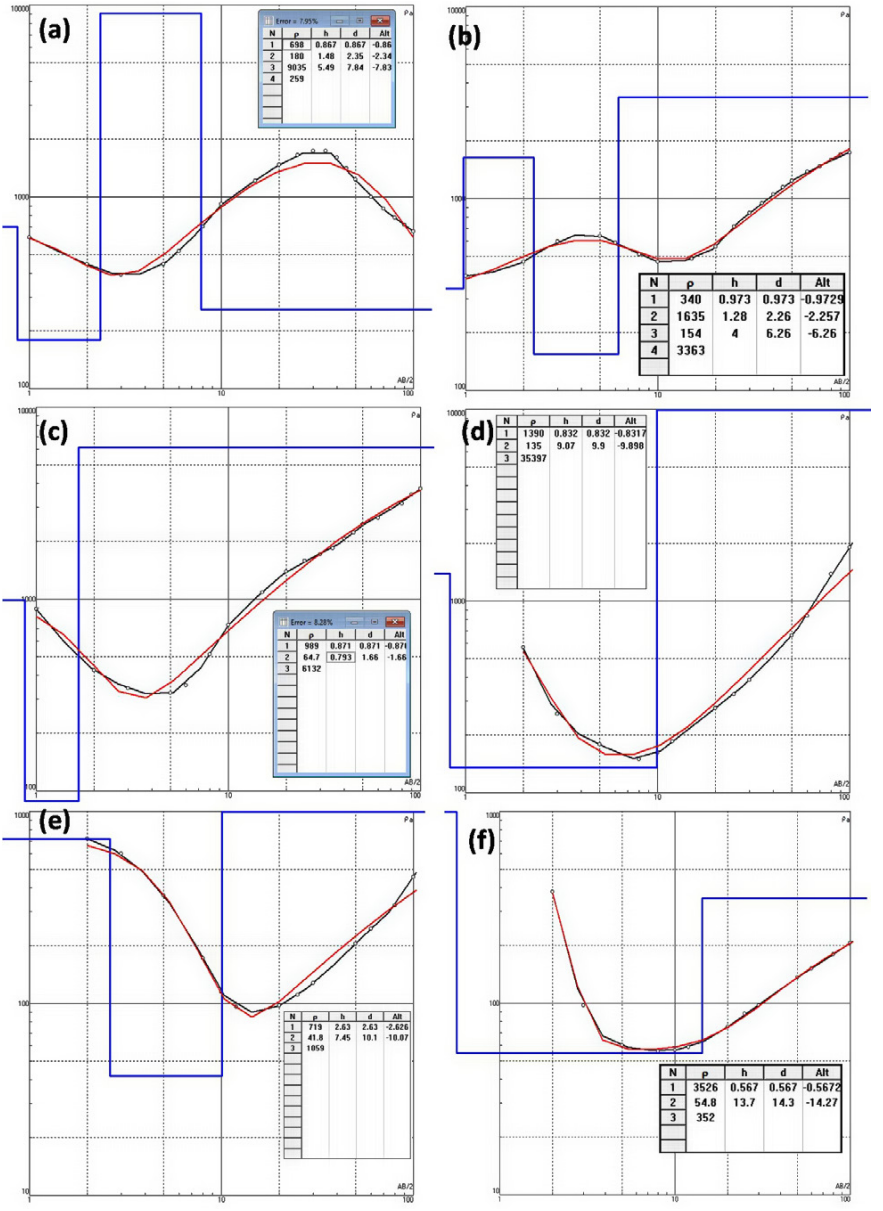

Fig. 10. Curves for (a) VES1, (b) VES2, (c) VES3, (d) VES4, (e) VES5, (f) VES6.

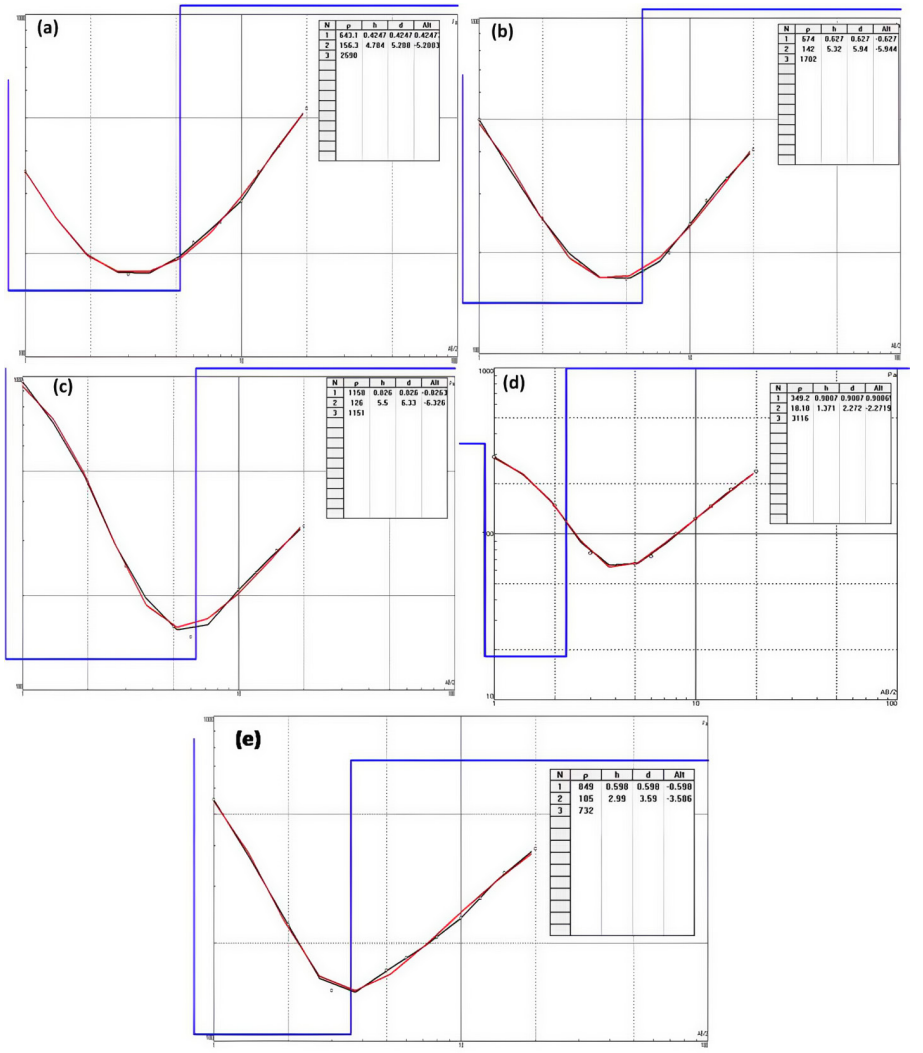

Fig. 11. Curves for (a) VES7, (b) VES8, (c) VES9, (d) VES10, (e) VES11.

layer is indicative of the extent of the underlying pegmatite. From Table 2, the depth to the pegmatite intrusive varies from 0.867 to 2.63 m, while the thickness ranges from 1.66 to 14.3 m.

Table 2. Lithologic log showing the different layers and thickness delineated based on VES derived-resistivity disparities.

VES no.	No. of layers	ρ (Ωm)	Thickness (m)	Depth (m)	Lithology
VES 1	4	698	0.867	0.867	crystalline rock
		180	1.48	2.35	weathered/fractured basement
		9035	5.49	7.84	fresh basement
		259	–	–	fractured basement
VES 2	4	340	0.973	0.973	crystalline rock
		1635	1.28	2.26	fresh basement
		154	4	6.26	fractured basement
		3363	–	–	fresh basement
VES 3	4	989	0.871	0.871	crystalline rock
		64.7	0.793	1.66	fractured basement
		6132	–	–	fresh basement
VES 4	3	1390	0.832	0.832	crystalline rock
		135	9.07	9.9	fractured basement
		35397	–	–	unweathered/fresh basement
VES 5	3	719	2.63	2.63	crystalline rock
		41.8	7.45	10.1	fractured basement
		1059	–	–	unweathered/fresh basement
VES 6	3	3526	0.567	0.567	crystalline rock
		54.8	13.7	14.3	fractured basement
		352	–	–	unweathered/fresh basement
VES 7	3	643.1	0.42	0.42	crystalline rock
		156.3	4.78	5.21	fractured basement
		2590	–	–	unweathered/fresh basement
VES 8	3	674	0.627	0.627	crystalline rock
		142	5.32	5.94	fractured basement
		1702	–	–	unweathered/fresh basement
VES 9	3	1158	0.826	0.826	crystalline rock
		126	5.55	6.33	fractured basement
		1151	–	–	unweathered/fresh basement
VES 10	3	349	0.9007	0.9007	weathered crystalline rock
		18.18	1.371	2.272	fractured basement
		3116	–	–	unweathered/fresh basement
VES 11	3	849	0.598	0.598	crystalline rock
		105	2.99	3.59	fractured basement
		732	–	–	unweathered/fresh basement

5. Discussion

To effectively identify target potential mineralisation zones, this research combines gravity, remote sensing, geochemistry, and resistivity data. The choice of the gravity technique is crucial. Majority of the related geophysical studies focus on the use of aeromagnetic surveys to map out structural trends; in contrast our study utilised the gravity technique, which is a novel application in the study area. By means of density contrast, the gravity survey mapped geological features and structures associated with mineral deposits. Potential zones for primary gold mineralisation were further confirmed based on the combination of gravity data with alterations extracted from Landsat data. Remote sensing was applied based on the premise that many gold mineralisations within the Nigerian basement complex have a proximal relationship to hydrothermal alterations. The host rocks have been hydrothermally altered to a quartz-sericite-annite-chlorite assemblage, which has become an indicator for Au-bearing rock ore (*Garba, 2003*). The band ratio maps showed distinct zones of clay and iron alterations, where bands 4/2, 6/5 and 6/7 maps display zones related to clay, ferric and ferrous iron alterations, respectively, which are associated with Au mineralisation (*Oke et al., 2014; Andongma et al., 2021*).

In addition, the gravity and remote sensing maps provided lineaments for both shallow and deeper density sources. The regional lineament trends from gravity and remote sensing data displayed a close affinity to hydrothermal alteration and gold mineralisation. These features serve as conduits for potential ore deposition from the ascending magmatic intrusions or the hydrothermal solutions (*Elkhateeb et al., 2021*). The lineaments exhibited a NS (north-south) trend along with less common NNW, NNE, NS, and WE trends. The dominant structural trend in the area is the NNE–SSW trending fault lines along which gold-mineralising fluids were possibly generated, channelled and deposited as gold-sulphide-quartz veins in the area. Similar structural trends have been reported in previous works. The faulting has been established as synchronous with Au mineralisation and hydrothermal alteration in several locations in Nigeria (*Garba, 2000*). The petrogenesis has been attributed to regional metamorphism. In their investigation of the mineralisation potentials of similar areas represented on Ilorin Sheet 223 using aero-radiomagnetic survey, *Bamigboye et al. (2023)* revealed a

NE–SW trending the northwest part of the area. It was concluded that the western half was more mineralised in metallic deposits such as gold because of the density of fractures in this area. Using aeromagnetic data, *Adebisi et al. (2024)* also identified high magnetic anomalies in the central, northeastern, and southeastern regions as prime targets for exploration, indicating magnetite-rich bodies, igneous intrusions, and hydrothermal zones. The study revealed structural trends mostly in the NE–SW direction, with some NW–SE alignments. *Lawal et al. (2024)* similarly reported that the area is dominated by structures trending NE–SW, NW, NE, EW and NS directions, although the structures trending NE–SW were found to be most predominant and considered as orientations of mineral deposits in the area. *Abraham et al. (2024)* reported that NE–SW and E–W trending faults control major mineralisation patterns in northcentral Nigeria. These structural trends were similarly observed on our maps, which supports the application of gravity and remote sensing maps in mineral exploration in the study area. The abovementioned studies all recommended the integration of geophysical, geochemical, and structural data in order to refine anomaly delineation, which is a key objective of this study.

The mapped locations were identified as target areas for exploration in the preliminary phase of mineral exploration in the Bielesen area of Asa in Kwara State. Hence, the delineated areas were then constrained using field and geochemical data. The geochemical studies indicate that Ag, Cu, Pb and Zn are associated with the gold mineralisation in the alteration zones and quartz veins. The study area presents average concentrations of Au mineralised zones associated with galena, sphalerite, monazite, bastnaesite, and manganese oxide minerals. The geochemical features of the rocks suggest that the potential gold mineralisation was structurally controlled, and the mechanism of Au transport and deposition is related to metamorphic processes. The gold might have been derived from the reworking or partial melting of the crustal igneous rocks (anatexis) during metamorphic changes. Likewise, some of the gold-mineralising fluids in NW Nigeria have been determined to be metamorphic in origin mainly through lithophile and rare earth elements characterization (*Garba, 2000; Danbatta et al., 2008*).TheAu deposits are understood to have formed through the precipitation of metamorphic fluids via devolatilization and dehydration processes (*Sanusi et al., 2024*). On the other hand, despite their relatively higher concentrations,

the base metals are by-products of wall rock alterations and might not economically recoverable.

The 3D Euler deconvolution maps indicate that the potential Au deposits in the study area occur with regions of intense tectonic deformation on the migmatite and biotite gneisses. The observed low resistivity is possibly associated with disseminated sulfide minerals that occur with auriferous quartz veins and fractured metasedimentary rocks, while the high resistivity values denote the presence of disseminated gold-sulfides within the quartz veins and fractured zones. From the interpretation of 3D Euler deconvolution and resistivity results as well as the trenching, the potential auriferous mineralised zones extend from the low-lying quartz veins and pegmatites at depths of approximately 1 m to deep-seated mineralisations at >1000 m.

6. Conclusion

This study entails a reconnaissance survey to identify geological indicators of mineralisation, and gravity and remote sensing investigations to delineate structures that serve as conduits for mineral emplacement. This work also provides a concise geochemical evaluation of mineralisation potential to ascertain the presence of viable ore deposits in the migmatite gneiss complex (MGC). The prominent anomalies observed on the residual Bouguer map were trending in the NE–SW direction. The gravity and band ratio maps were able to delineate basement highs and lows, as well as areas of potential mineralisation. The field work identified the host rock as migmatite gneiss. The mineralogical composition includes quartz, feldspar and tourmaline. The presence of leucosomes is suggestive of epithermal formation of the mineral deposits. The minerals occur as discrete grains disseminated in pegmatite and veins. The geological controls for the hosting and emplacement of the mineralisation are structural (faults, fractures) as confirmed by the Bouguer anomaly maps, Landsat images and field occurrences. The estimated depth could help in tonnage estimation as well as the equipment requirement for excavation activities. The results suggest gold mineralisation potential in the study area. The results provide a viable premise for detailed investigations. Without this methodical approach to exploration, the mineral resources can have the potential of causing environmental degradations through high incidents of dry holes.

Acknowledgements. The study whose part of its results is presented in this work is funded by the TET Fund under the 2024 Institutional based Research (NRF) Fund.

Conflict of interest statement. (i) All authors agree with the submission, (ii) the work has not been published elsewhere, either completely, in part, or in another form and (iii) the manuscript has not been submitted to another journal.

References

Abdelrahman K., El-Qassas R. A. Y., Fnais M. S., Andráš P., Eldosouky A. M., 2023: Geological Structures Controlling Au/Ba Mineralization from Aeromagnetic Data: Harrat ad Danun Area, Saudi Arabia. Minerals, **13**, 7, 866, doi: 10.3390/min13070866.

Abraham E. M., Uwaezuoke A. E., Usman A. O., 2024: Geophysical investigation of subsurface mineral potentials in North-Central Nigeria: implications for sustainable mining and development. Geomech. Geophys. Geo-Energy Geo-Res., **10**, 1, 192, doi: 10.1007/s40948-024-00913-3.

Adebisi W. A., Folorunso I. O., Abubakar H. O., Olatunji S., Olaojo M. O., 2024: Delineating Structural Features Related to Hydrothermal Alterations for Possible Mineralization in Share Area, Kwara State Nigeria Using Aeromagnetic Data. Indones. J. Earth Sci., **4**, 2, A1265, doi: 10.52562/injoes.2024.1265.

Adekoya J. A., 1991: The geology of the banded iron – formation in the Precambrian Basement Complex of northern Nigeria. Unpubl. Ph.D. Thesis. University of Ibadan, Nigeria. 395 p.

Adekoya J. A., Kehinde-Phillips O. O., Odukoya A. M., 2003: Geological distribution of mineral resources in southwestern Nigeria. In: Elueze A. A. (Ed.): Prospects for investment in mineral resources of southwestern Nigeria. Nigerian Mining and Geosciences Society, 1–13.

Ajadi J., Dada S. S., Nnabo P. N., Owoeye B. A., 2018: Lithostructural description and metalogeny of Alagbede gold deposit, West Central Nigeria. J. Environ. Earth Sci., **8**, 5, 115–132.

Ajibade A. C., Woakes M., Rahaman M. A., 1987: Proterozoic crustal development in the Pan-African regime of Nigeria. In: Kröner A. (Ed.): Proterozoic lithospheric evolution (Geodynamics Series, Vol. 17). American Geophysical Union, Washington, D.C., USA, pp. 259–271.

Alarifi S. S., El-Qassas R. A. Y., Omar A. E. A., Al-Saleh A. M., Andráš P. Eldosouky A. M., 2024: Remote sensing and aeromagnetic mapping for unveiling mineralization potential: Nuqrah Area, Saudi Arabia. Geomech. Geophys. Geo-Energy Geo-Res., **10**, 1, 149, doi: 10.1007/s40948-024-00844-z.

Ali A. S. O., Pour A. B., 2014: Lithological mapping and hydrothermal alteration using Landsat 8 data: a case study in ariab mining district, red sea hills, Sudan. Int. J. Basic Appl. Sci., **3**, 3, 199–208, doi: 10.14419/ijbas.v3i3.2821.

Andongma W. T., Gajere J. N., Amuda A. K., Rwabuhungu Rwatangabo D. E., Faisal M., Yusuf Y. D., 2021: Mapping of hydrothermal alterations related to gold min-

eralization within parts of the Malumfashi Schist Belt, North-Western Nigeria. Egypt. J. Remote Sens. Space Sci., **24**, 3, Part 1, 401–417, doi: 10.1016/j.ejrs.2020.11.001.

Balogun O. B., 2019: Tectonic and structural analysis of the Migmatite–Gneiss–Quartzite complex of Ilorin area from aeromagnetic data. NRIAG J. Astron. Geophys., **8**, 1, 22–33, doi: 10.1080/20909977.2019.1615795.

Bamigboye O. S., Bamidele T. E., Omorinoye O. A., Adeboye J. O., 2023: Assessment of mineralization potential of areas represented on Ilorin Sheet 223, Southwestern Nigeria from aeromagnetic and aeroradiometric analyses. J. Min. Geol., **59**, 2, 117–129.

Bencharef M. H., Eldosouky A. M., Zamzam S., Boubaya D., 2022: Polymetallic mineralization prospectivity modelling using multi-geospatial data in logistic regression: The Diapiric Zone, Northeastern Algeria. Geocarto Int., **37**, 27, 15392–15427, doi: 10.1080/10106049.2022.2097481.

Cooper G. R. J., Cowan D. R., 2004: Filtering using variable order vertical derivatives. Comput. Geosci., **30**, 5, 455–459, doi: 10.1016/j.cageo.2004.03.001.

Cordell L., Grauch V. J. S., 1985: Mapping basement magnetization zones from aeromagnetic data in the San Juan basin, New Mexico. In: Hinze W. J. (Ed.): The utility of regional gravity and magnetic anomaly maps. Society of Exploration Geophysicists (SEG), Tulsa, OK, pp. 181–197.

Dada S., Ajadi J., 2018: Exploiting Kwara State Mineral Resources for Economic Sustainability. In: Musa A. (Ed.): Kwara at 50: Achievements and Aspirations. Fifty-Fifty Institute Ltd., pp. 123–137.

Danbatta U. A., Abubakar Y. I., Ibrahim A. A., 2008: Geochemistry of Gold Deposits in Anka Schist Belt, Northwestern, Nigeria. Niger. J. Chem. Res., **13**, 19–29.

Daud Y., Sulistyo A., Fahmi F., Nuqramadha W. A., Fitrianita, Sesesega R. S., Rosid S., Pati G. P., Maulana M. R., Khoiroh M., Rahman K. R., Subroto W., 2019: First horizontal derivative and Euler Deconvolutionin application for reconstructing structural signature over the Blawan-Ijen Geothermal area. IOP Conf. Ser.: Earth Environ. Sci., **254**, 012008, doi: 10.1088/1755-1315/254/1/012008.

Ekwok S. E., Akpan A. E., Achadu O.-I. M., Thompson C. E., Eldosouky A. M., Abdelrahman K., András P., 2022: Towards Understanding the Source of Brine Mineralization in Southeast Nigeria: Evidence from High-Resolution Airborne Magnetic and Gravity Data. Minerals, **12**, 2, 146, doi: 10.3390/min12020146.

Eldosouky A. M., Abdelkareem M., Elkhateeb S. O., 2017: Integration of remote sensing and aeromagnetic data for mapping structural features and hydrothermal alteration zones in Wadi Allaqi area, South Eastern Desert of Egypt. J. Afr. Earth Sci., **130**, 28–37, doi: 10.1016/j.jafrearsci.2017.03.006.

Eldosouky A. M, El-Qassas R. A. Y., Pham L. T., Abdelrahman K., Alhumimidi M. S., El Bahrawy A., Mickus K., Sehsah H., 2022: Mapping Main Structures and Related Mineralization of the Arabian Shield (Saudi Arabia) Using Sharp Edge Detector of Transformed Gravity Data. Minerals, **12**, 1, 71, doi: 10.3390/min12010071.

Eldosouky A. M., Pham L. T., El-Qassas R. A.Y., Kieu T. D., Mohamed H., Le C. V. A., 2023: 5 – Geophysical data for mineral exploration. In: Pour A. B., Parsa M.,

Eldosouky A. M. (Eds.): Geospatial Analysis Applied to Mineral Exploration. Elsevier, 189–231, doi: 10.1016/B978-0-323-95608-6.00005-6.

Eldosouky A. M., Othman A., Saada S. A., Zamzam S., 2024a: A New Vector for Mapping Gold Mineralization Potential and Proposed Pathways in Highly Weathered Basement Rocks using Multispectral, Radar, and Magnetic Data in Random Forest Algorithm. Nat. Resour. Res., **33**, 1, 23–50, doi: 10.1007/s11053-023-10292-3.

Eldosouky A. M., Eleraki M., Mansour A., Saada S. A., Zamzam S., 2024b: Geological controls of mineralization occurrences in the Egyptian Eastern Desert using advanced integration of remote sensing and magnetic data. Sci. Rep., **14**, 16700, doi: 10.1038/s41598-024-66924-y.

Elkhateeb S. O., Eldosouky A. M., Khalifa M. O., Aboalhassan M., 2021: Probability of mineral occurrence in the Southeast of Aswan area, Egypt, from the analysis of aeromagnetic data. Arab. J. Geosci., **14**, 15, 1514, doi: 10.1007/s12517-021-07997-1.

Epuh E. E., Joshua E. O., 2017: Gongola Basin Crust-Mantle Structural Analysis For Hydrocarbon Investigation Using Isostatic Residual Gravity Anomalies. Niger. J. Basic Appl. Sci., **25**, 2, 51–65, doi: 10.4314/njbas.v25i2.7.

Fairhead J. D., Williams S. E., Flanagan G., 2004: Testing magnetic local wavenumber depth estimation methods using a complex 3D test model. SEG Technical Program Expanded Abstracts, 742–745, doi: 10.1190/1.1851313.

Fedi M., Florio G., 2001: Detection of potential fields source boundaries by Enhanced Horizontal Derivative method. Geophys. Prospect., **49**, 1, 40–58, doi: 10.1046/j.1365-2478.2001.00235.x.

Fedi M., Florio G., 2002: A stable downward continuation by using the ISVD method. Geophys. J. Int., **151**, 1, 146–156, doi: 10.1046/j.1365-246X.2002.01767.x.

Gabr S. S., Diab H., Abdel Fattah T. A., Sadek M. F., Khalil K. I., Youssef M. A. S., 2022: Aeromagnetic and Landsat-8 data interpretation for structural and hydrothermal alteration mapping along the Central and Southern Eastern Desert boundary, Egypt. Egypt. J. Remote Sens. Space Sci., **25**, 1, 11–20, doi: 10.1016/j.ejrs.2021.12.002.

Garba I., 2000: Origin of Pan-African mesothermal gold mineralization at Bin Yauri, Nigeria. J. Afr. Earth Sci., **31**, 2, 433–449, doi: 10.1016/S0899-5362(00)00098-1.

Garba I., 2003: Geochemical characteristics of mesothermal gold mineralization in the Pan-African (600 ±150 Ma) basement of Nigeria. Appl. Earth Sci., **112**, 3, 319–325, doi: 10.1179/037174503225003143.

Hamimi Z., Eldosouky A. M., Hagag W., Kamh S. Z., 2023: Large-scale geological structures of the Egyptian Nubian Shield. Sci. Rep., **13**, 1923, doi: 10.1038/s41598-023-29008-x.

Imbroane M. A., Melenti C., Gorgan D., 2007: Mineral Explorations by Landsat Image Ratios. In: Proc. Ninth International Symposium on Symbolic and Numeric Algorithms for Scientific Computing (SYNASC 2007), Timisoara, Romania, September 26–29, 2007, pp. 335–340, doi: 10.1109/SYNASC.2007.52.

Knoll T., Huet B., Schuster R., Mali H., Ntaflos T., Hauzenberger C., 2023: Lithium pegmatite of anatectic origin – A case study from the Austroalpine Unit Pegmatite

Province (Eastern European Alps): Geological data and geochemical modeling. Ore Geol. Rev., **154**, 105298, doi: 10.1016/j.oregeorev.2023.105298.

Lawal T. O., Jimoh A. A., Omar D. M., Fawale O., Abayomi J. S., 2024: Delineation of structural features and hydrothermal alteration zones using integrated geophysical data of part of North-central Nigeria. Proc. Niger. Soc. Phys. Sci., **1**, 1, 83, doi: 10.61298/pnspsc.2024.1.83.

McCurry P., 1976: The Geology of the Precambrian to Lower Paleozoic Rocks of Northern Nigeria—A Review. In: Kogbe C. A. (Ed.): Geology of Nigeria. Elizabethan Publ. Co., Lagos, Nigeria, pp. 15–39.

Miller H. G., Singh V., 1994: Potential field tilt—a new concept for location of potential field sources. J. Appl. Geophys., **32**, 2-3, 213–217, doi: 10.1016/0926-9851(94)90022-1.

Moghaddam M. M, Sabseparvar M., Mirzaei S., Heydarian N., 2015: Interpretation of Aeromagnetic Data to Locate Buried Faults in North of Zanjan Province, Iran. J. Remote Sens. GIS, **4**, 2, 143, doi: 10.4172/2469-4134.1000143.

Obiora S. C., Ukaegbu V. U., 2009: Petrology and geochemical characteristics of Precambrian granitic basement complex rocks in the southernmost part of North-Central Nigeria. Chin. J. Geochem., **28**, 4, 377–385, doi: 10.1007/s11631-009-0377-2.

Odeyemi I., 1981: A review of the orogenic events in the Precambrian basement of Nigeria, West Africa. Geol. Rundsch., **70**, 3, 897–909, doi: 10.1007/BF01820170.

Oke S. A., Abimbola A. F., Rammlmair D., 2014: Mineralogical and Geochemical Characterization of Gold Bearing Quartz Veins and Soils in Parts of Maru Schist Belt Area, Northwestern Nigeria. J. Geol. Res., **2014**, 314214, doi: 10.1155/2014/314214.

Ousmanou S., Fodoue Y., Wadjou J. W., Kepnamou A. D., Fozing E. M., Kwékam M., Ikfi M., 2024: Fuzzy-logic technique for gold mineralization prospecting using Landsat 9 OLI processing and fieldwork data in the Bibemi goldfield, north Cameroon. Heliyon, **10**, 1, e23334, doi: 10.1016/j.heliyon.2023.e23334.

Oyawoye M. O., 1972: The Basement Complex of Nigeria. In: Dessauvagie T. F. J., Whiteman A .J. (Eds.): African Geology. Ibadan University Press, Ibadan, pp. 67–99.

Paterson N. R., Reeves C. V., 1985: Applications of gravity and magnetic surveys: The state-of-the-art in1985. Geophysics, **50**, 12, 2558–2594, doi: 10.1190/1.1441884.

Pham L. T., Oliveira S. P., Le-Huy M., Nguyen D. V., Nguyen-Dang T. Q., Do T. D., Tran K. V., Nguyen H.-D. T., Ngo T.-N. T., Pham H. Q., 2024: Reliable Euler deconvolution solutions of gravity data throughout the β-VDR and THGED methods: Application to mineral exploration and geological structural mapping. Vietnam J. Earth Sci., **46**, 3, 432–448, doi: 10.15625/2615-9783/21009.

Pham L. T., 2025: A generalized β-VDR method for computing high-order vertical derivatives: application to downward continuation. Geophys. J. Int., **243**, 2, ggaf334, doi: 10.1093/gji/ggaf334.

Pour A. B., Hashim M., Hong J. K., Park Y., 2019: Lithological and alteration mineral mapping in poorly exposed lithologies using Landsat-8 and ASTER satellite data: North-eastern Graham Land, Antarctic Peninsula. Ore Geol. Rev., **108**, 112–133, doi: 10.1016/j.oregeorev.2017.07.018.

Ramadan T. M., Abdel Fattah M. F., 2010: Characterization of gold mineralization in Garin Hawal area, Kebbi State, NW Nigeria, using remote sensing. Egypt. J. Remote Sens. Space Sci., **13**, 2, 153–163, doi: 10.1016/j.ejrs.2009.08.001.

Reid A. B., Allsop J. M., Granser H., Millet A. J., Somerton I. N., 1990: Magnetic interpretation in three dimensions using Euler deconvolution. Geophysics, **55**, 1, 80–91, doi: 10.1190/1.1442774.

Reid A. B., Ebbing J., Webb S. J., 2014: Avoidable Euler Errors – the use and abuse of Euler deconvolution applied to potential fields. Geophys. Prospect., **62**, 5, 1162–1168, doi: 10.1111/1365-2478.12119.

Rye D. M., Rye R. O., 1974: Homestake Gold Mine, South Dakota: I. Stable Isotope Studies. Econ. Geol., **69**, 3, 293–317, doi: 10.2113/gsecongeo.69.3.293.

Sanusi S. O., Josiah, D. I.-A., Olaniyan O., Olayanju G. M., 2024: Delineation of Potential Gold Mineralization Zones in the Kushaka Schist Belt, Northcentral Nigeria, Using Geochemical, Ground Magnetic, Induced Polarization, and Electrical Resistivity Methods. Mining Metall. Explor., **41**, 4, 2007–2029, doi: 10.1007/s42461-024-01033-y.

Smith R. S., Thurston J. B., Dai T.-F., MacLeod I. N., 1998: iSPI^{TM} – the improved source parameter imaging method. Geophys. Prospect., **46**, 2, 141–151, doi: 10.1046/j.1365-2478.1998.00084.x.

Taylor S. R., McLennan S. M., 1985: The Continental Crust: Its Composition and Evolution. Blackwell Scientific Publications, Oxford, 312 p.

Thompson D. T., 1982: EULDPH: A new technique for making computer-assisted depth estimates from magnetic data. Geophysics, **47**, 1, 31–37, doi: 10.1190/1.1441278.

Thurston J. B., Smith R. S., 1997: Automatic conversion of magnetic data to depth, dip, and susceptibility contrast using the SPI (TM) method. Geophysics, **62**, 3, 807–813, doi: 10.1190/1.1444190.

Turner D. C., 1983: Upper Proterozoic schist belts in the Nigerian sector of the Pan-African province of West Africa. Precambrian Res., **21**, 1-2, 55–79, doi: 10.1016/0301-9268(83)90005-0.

Vander Velpen B. P. A., 2004: WinRESIST version 1.0 resistivity depth sounding interpretation software. M.Sc. Research Project, ITC, Delft, the Netherland.

Whitehead N., Musselman C., 2005: Montaj^{TM} Grav/Mag interpretation: Processing, analysis and visualization system for 3D inversion of potential field data for Oasis montaj v6.1. Geosoft Inc., ON, Canada.

Woakes M., Bafor B. E., 1984: Primary gold mineralization in Nigeria. In: Foster R. P. (Ed.): Proc. Gold '82 symposium: The geology geochemistry and genesis of gold deposits. A. A. Balkema, Rotterdam, pp. 661–671.

Wright J. B., Hastings D. A., Jones W. B., Williams H. R., 1985: Geology and Mineral Resources of West Africa. Allen and Unwin, London, 187 p.